Chapter 7

Determination of the Bulk and Local Diffusion-Length Values of Charge Carriers in MCT Films and in the Absorber Layers of MCT-Based Photovoltaic IR FPA Detectors

S.A. Dvoretsky, V.V. Vasil'ev, A.V. Predein, A.V. Vishnyakov, V.A. Stuchinsky, D.V. Brunev and A.V. Zverev

Additional information is available at the end of the chapter

http://dx.doi.org/10.5772/60717

Abstract

In the present chapter, we describe two new photoelectric-measurement-based methods that can be used for characterization of the diffusion process of charge carriers either in mercury-cadmium-tellurium (MCT) films intended for fabrication of infrared focal plane array (IR FPA) detectors or in the absorber layers of ready MCT-based photovoltaic IR FPA detectors. First-type measurements are photocurrent measurements to be performed on special test structures involving round photodiodes provided with coaxial light-shielding cap metal contacts. Second-type measurements are spot-scan measurements of MCT photovoltaic 2D IR FPA detectors traditionally used for measuring the crosstalk value of such detectors yet implemented at low and high levels of registered diode photocurrents. Both methods permit the determination of the bulk diffusion length of minority charge carriers in MCT material. The second method, in addition, permits the determination of the local effective diffusion length of minority charge carriers in the absorber-layer region under FPA diodes. The values of the bulk diffusion length of minority carriers obtained in MCT films and in the MCT absorber material of the examined middle-wave and long-wave IR FPA detectors were found to be in good agreement with previously reported relevant data. The estimated value of the local effective diffusion length of minority carriers in the film region under back-biased FPA diodes proved to be consistent with a theoretical estimate of this length.

Keywords: infrared focal plane array detectors, mercury-cadmium-tellurium, diffusion, diffusion length, charge carriers, test structures, spot-scan measurements

1. Introduction

In infrared (IR) imaging and detection, cooled hybrid mercury-cadmium-tellurium (MCT) photovoltaic IR focal plane array (FPA) detectors have found widespread use [1, 2]. Collection of photogenerated charge carriers by FPA diodes in the photodiode arrays of such detectors is a process essentially mediated by the diffusion of minority carriers in the MCT film. That is why the performance characteristics of MCT IR FPA detectors and their figures of merit depend on the distances the excess carriers diffuse over in the photosensitive film (PF) of such detectors [3, 4]. Among the parameters that govern the diffusion process, of primary interest is the bulk diffusion length of minority charge carriers l_d in the absorber material of the detector as this length characterizes the properties of the material irrespective of a particular FPA design, including the pixel architecture and array structure. Knowledge of l_d is significant for quantitative analysis and numerical modeling of FPA detectors. With known mobility of minority carriers, this knowledge also permits evaluation of the lifetime of excess carriers in MCT, which is often hard to measure because of its small value. Finally, the length l_d is generally regarded as a key parameter that defines the crosstalk value of FPA detectors [5-9].

In view of the aforesaid, of considerable interest are new experimental techniques and analysis methods that can be used for determining the length l_d in the MCT material of MCT-based films and diode hetero-epitaxial structures.

In the present chapter, we describe two new photoelectric-measurement-based methods that can be used for characterization of the diffusion process of charge carriers either in MCT films intended for fabrication of IR FPA detectors or in the absorber layers of ready MCT-based photovoltaic IR FPA detectors. Both methods permit the determination of the bulk diffusion length of minority charge carriers l_d in MCT material.

First-type photoelectric measurements can be performed on special test structures involving round photodiodes of radius r_0 provided with coaxial light-shielding cap metal contacts of different radii $R_i > r_0$. The contacts shield the vicinity of the photodiodes from the excitation radiation falling onto the front surface of the test structure. In the shielded region, the optical generation of excess charge carriers is nearly zero, and the diode photocurrents are therefore formed by those minority carriers that reach the diode via diffusion across the shielded annular region of width $R_i - r_0$. Numerically solving an appropriate 2D diffusion problem, we can preliminarily calculate the diode photocurrents I_i as a function of l_d for several experimentally implemented values of $R_i - r_0$. To avoid the necessity of performing absolute measurements and calculations, photocurrent ratios I_1/I_2, I_1/I_3, I_1/I_4, etc. for diode pairs with different contact-to-diode size ratios can be calculated. Then, the calculated curves I_1/I_i (l_d) can be used as reference dependences allowing the determination of the length l_d in the MCT film under study.

http://dx.doi.org/10.5772/60717

Second-type measurements are spot-scan measurements of MCT photovoltaic 2D IR FPA detectors traditionally used for measuring the crosstalk value of such detectors, yet implemented at low levels of registered diode photocurrents j_{ph}. Low photocurrent levels can be achieved by lowering the gate potential V_g of input field effect transistors (FETs) in the readout circuits of the photoelectric cells of the detector. The requirement for low values of the photocurrents j_{ph} extracted by the readout circuits out of the photosensitive film of the detector arises as a condition for minimization of the influence of readout circuits on the lifetime and the effective (at $j_{ph} \neq 0$) diffusion length of photogenerated minority carriers in the photosensitive film $l_{d\ eff}$. The effective diffusion lengths $l_{d\ eff}$ can be extracted from broadened spatial diode photoresponse profiles $S(x)$ registered on successive reduction of the level of registered diode photocurrents. Then, the bulk diffusion length of minority charge carriers in the photosensitive film l_d can be found as the extreme value of $l_{d\ eff}$ as $j_{ph} \rightarrow 0$. For revealing the asymptotic behavior of $l_{d\ eff} \rightarrow l_d$ for $j_{ph} \rightarrow 0$, a special diffusion model with zero PF thickness was developed. This model was subsequently used to analyze the charge-carrier diffusion process at normal operational regime of the detector with large diode photocurrents j_{ph}. The latter analysis has allowed us to evaluate the local diffusion length of minority charge carriers in the PF region under the back-biased FPA diodes $l_{d\ eff}$. The obtained value of this length proved to be in good agreement with a theoretical estimate of this length. As a result, an experimental approach enabling a comprehensive spot-scan characterization of the charge-carrier diffusion process in the absorber layers of MCT IR FPA detectors at arbitrary levels of diode photocurrents has been developed.

2. A method for determining the diffusion length of minority charge carriers in MCT films with band-graded surface layers

The method for determining the diffusion length of minority carriers in MCT films l_d (or L_n, for electrons in *p*-type semiconductor) is based on the previously mentioned fact that this length presents an important parameter that defines, among other characteristics, the quantum efficiency of lateral diode structures prepared on such films [4].

2.1. Essence of the method

Methods for determining the lateral optical collection length of charge carriers l_{opt} in MCT films based on quantum-efficiency measurements of lateral diode structures comprising variable-area diode arrays have previously been reported in the literature (see, for instance, [10, 11]). The procedure for determining the length l_{opt} in those methods is based on the fact that measured quantum efficiency of back-biased photodiodes in such structures is essentially defined, first, by the diffusion length of minority charge carriers l_{opt} and, second, by the diode radius. However, measured length l_{opt} presents only a rough estimate to the diffusion length of minority carriers in the film.

In [12], we have proposed another method for determining the length l_d in photosensitive semiconductors. That method was subsequently implemented to perform measurements of

the electron diffusion length L_n in *p*-type MCT-film-based hetero-epitaxial structures [13]. The proposed method uses the fact that measured photocurrent produced by an illuminated *p-n* junction capped with a coaxial light-shielding metal contact varies in magnitude as we change the radius of the *n*-type region of the diode r_0 and/or the radius of the cap contact *R*. Of course, the radius r_0 is always smaller than *R*. A schematic of such a photodiode is shown in Fig. 1. The method works as follows. First, we measure the ratio between the photocurrents produced by two photodiodes having different values of R-r_0. Preliminarily, the photocurrent ratio is theoretically calculated to be plotted versus the electron diffusion length L_n. Then, with the measured photocurrent ratios at hand, we can use the theoretically calculated curves as reference dependences from which the length L_n can be determined.

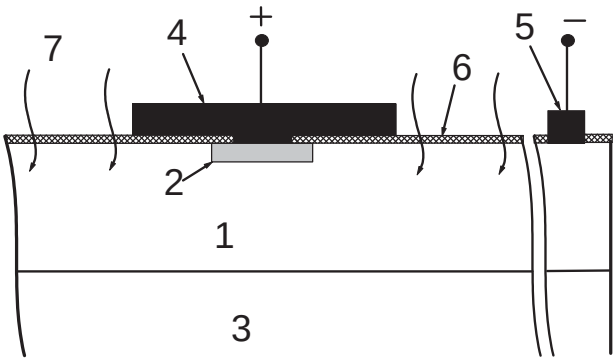

Figure 1. Schematic of a photodiode provided with a coaxial light-shielding cap contact. 1 – *p*-type MCT film, 2 – *n*-type diode region of radius r_0, 3 – substrate, 4 – shielding contact of radius *R* to the *n*-type region, 5 – peripheral contact to the *p*-type MCT film, 6 – dielectric, 7 – illumination.

2.2. Calculations

The photocurrent produced by a *p-n* photodiode was calculated by numerically solving the 2D stationary continuity equation for excess electron concentration in an axisymmetric quasi-neutral *p*-type region in the vicinity of the *p-n* diode illuminated, from the side of the cap contact, with an IR radiation flux that modeled the radiation flux used in the experiment. With the electron mobility and the electron lifetime assumed constant, the continuity equation has the form

$$\frac{\partial^2 n'}{\partial r^2} + \frac{1}{r}\frac{\partial n'}{\partial r} + \frac{\partial^2 n'}{\partial z^2} - \frac{1}{L_n^2}\cdot n' = -\frac{g(z,r)}{D_n} \tag{1}$$

In Eq. (1), the *z* axis is directed along the symmetry axis of the photodiode normally to the *p*-type absorber layer, and the *r* axis is directed along radius; $n' = n - n_{p0}$ is the concentration of minority carriers in excess of their equilibrium concentration n_{p0}, D_n is the electron diffusion

http://dx.doi.org/10.5772/60717

constant in the *p*-type absorber material, and *g(z,r)* is a function that describes the rate of photogeneration of charge carriers in the illuminated film with allowance for the shielding action of the cap contact:

$$g(z,\ r)=F(r)\int_0^{\lambda_1}\alpha(\lambda)Q(\lambda)\exp(-\alpha z)d\lambda$$

Here, $\alpha(\lambda,z)$ is the absorption coefficient, $Q(\lambda,\ T_b)=\frac{2\pi c}{\lambda^4[\exp(hc/\lambda kT_b)-1]}$ is the Planck distribution function for the blackbody emissivity at temperature T_b (see, for instance, [1]), $\lambda_1 \approx 20$ μm is a wavelength far exceeding the long-wave cutoff wavelength λ_c of the *p*-type MCT absorber layer, and *F(r)* is the shielding function (in a simplest model, $F(r)=0$ for $r < R$ and $F(r)=1$ for $r > R$). Since, in what follows, ratios of diode-produced photocurrents will be calculated, then the knowledge of the absolute value of the radiation flux (which depends on the aperture angle and on the coefficient of radiation reflection from the surface of the test structure) is not necessary. The absorption coefficient α depends on the coordinate across the photosensitive film since, starting from a distance 0.4 μm from either the lower or upper surface of the film, the cadmium content of the MCT material and, hence, its bandgap energy in the test structure gradually increase in value toward the surface. The graded-band MCT surface layers were used to suppress the surface recombination of excess carriers at the surface boundaries of the *p*-type MCT film [14]. The computational domain in which Eq. (1) was solved is shown in Fig. 2. This domain is the region referring to the coordinate ranges $r=0\div R_{ph}$ and $z=0\div H$; the $Cd_xHg_{1-x}Te$ material in this domain has fixed composition *x*.

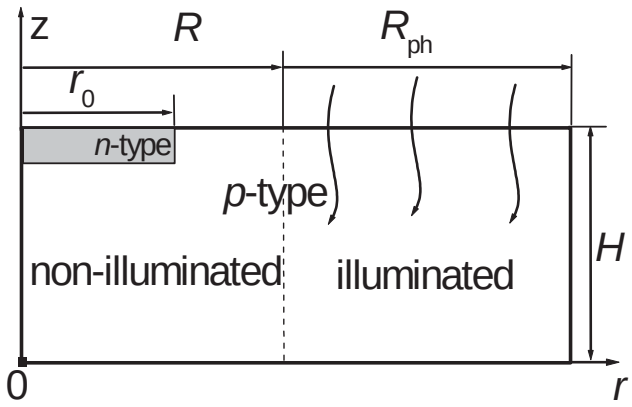

Figure 2. Computational domain.

In solving the continuity equation, the following boundary conditions were adopted [15]:

a. $\frac{\partial n'}{\partial r}=0$ for $r = 0$ and on the lateral cylindrical surface of the computational domain at $r = R_{ph} = r_0 + 5L_{n,\,max}$, where $L_{n,\,max}$ is the maximum value of L_n for which the computations were performed, and r_0 is the radius of the *p-n* junction.

b. $n' = n_{p0}(\exp(qV/kT) - 1)$ – on the lateral and planar surfaces of the *p-n* junction; here, V is the voltage bias across the diode, q is the electron charge, k is the Boltzmann constant, and T is temperature. In calculating the photocurrent, the bias voltage was assumed to be zero.

c. $D_n \frac{\partial n'}{\partial z} = S_r n'$ – on the upper and lower boundaries of the base layer at $z = 0$ and $z = H$, where S_r is the effective rate of recombination of minority carriers at those surfaces.

With regard to the data of [16], the electron mobility value μ_n=6×10^4 cm^2/V×s for *p*-type $Cd_xHg_{1-x}Te$ with x=0.223 was adopted in the calculations. The bandgap energy E_g and the intrinsic concentration of charge carriers n_i in the MCT material were calculated as functions of MCT-material stoichiometry and temperature by the formulas borrowed from the monograph [1]. The MCT absorption coefficient was calculated using the formulas reported in [17]. In the calculations, the length L_n was varied by changing the electron lifetime τ_n according to the formula $L_n=(D_n\,\tau_n)^{1/2}$. Equation (1) was transformed in a finite-difference equation to be solved, by the sweep method, on a grid with variable step over the *p*-type region. The total number of applied iterations reached 15000. The photocurrents across the planar and lateral surfaces of the *p-n* junction, $j_N = qD_n\frac{\partial n}{\partial z}$ and $j_L = qD_n\frac{\partial n}{\partial r}$, were calculated via numerical differentiation of the obtained solution $n'(r,z)$. The integral diode photocurrent I was calculated by numerical integration of photocurrent density over the *p-n* junction surface.

2.3. Experimental

For experimental implementation of the method, a test photodiode structure whose fragment is shown in Fig. 3 was fabricated.

In the fabricated structure, the radius of the *p-n* junctions was fixed, equal to $r_0 \approx 6.5$ μm, whereas the radius of the shielding contacts varied in the range from 10 to 100 μm (see Fig. 3 and Table 1). The distance between neighbor diodes was chosen to be sufficiently large, so that their contacts exerted no influence on the photocurrents produced by the neighbor diodes. At the periphery of the lateral diode structure, a second contact (to the *p*-type absorber layer) was provided. Diode photocurrents were determined from measured current-voltage characteristics of illuminated and nonilluminated diodes. The characteristics were measured with the help of a thin probe brought in contact to the diode caps. The structure of each individual lateral photodiode involved a peripheral metal-insulator-semiconductor (MIS) region formed by the cap metal contact, by the dielectric, and by the *p*-type MCT material (see Fig. 1). For avoiding the formation of surface inversion layers in the vicinity of the diodes, a sufficiently thick dielectric layer without a noticea-

http://dx.doi.org/10.5772/60717

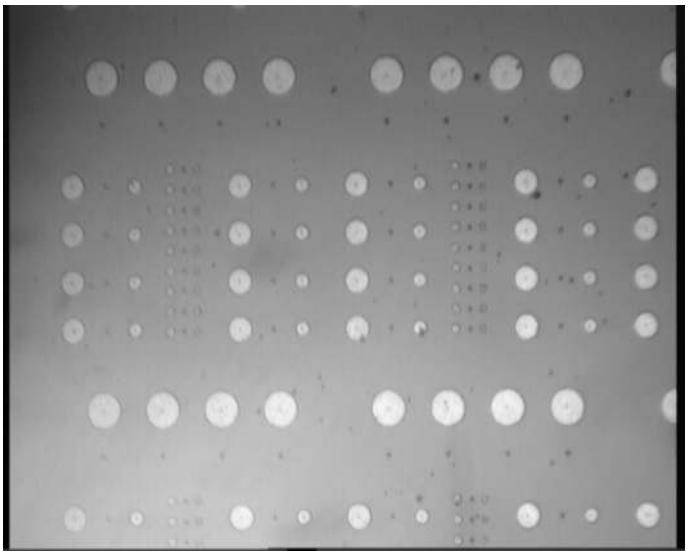

Figure 3. Fragment of the test structure. The test structure comprises photodiode sets with different diameters of cap contacts. In the photo, the structure is shown as viewed from the side of the cap contacts, which appear as light round regions.

ble positive built-in charge and, also, a metal with a work function value close to that of the semiconductor need to be used, and measurements are to be performed on diodes biased with a sufficiently low bias voltage. In the test structures used in our experiments, a 0.15-μm thick double-layer SiO_2/Si_3N_4 dielectric and indium metallization, allowing one to meet the above-formulated requirements, were used. In the experiments, a test structure fabricated on a variband MCT film grown on a GaAs substrate was placed on the surface of a corundum ceramic plate. The plate was cooled down to T=78 K, via a copper cylinder, by liquid nitrogen into which the copper cylinder was immersed. The ceramic plate was necessary for preventing the reflection of IR radiation having passed through the thin MCT layer and through the transparent GaAs plate, from the metal surface of the cylinder. Such reflection could otherwise entail additional absorption of reflected radiation in the MCT material under the shielding contact, which was neglected in our calculations, and, hence, it could result in an increased value of measured photocurrent. The latter in turn could induce an additional inaccuracy in the found value of L_n. The illumination of the test structure was performed from the side of the cap contacts by exposing the sample to 293-K thermal background radiation passing through an aperture angle of 32°. The test structure was fabricated on sample 1-MCT130607 with the following characteristics of the p-type MCT film: thickness 8 μm, stoichiometric coefficient x=0.223, hole mobility μ_p= 540 $cm^2/V\times s$, hole concentration p=6.7×10^{15} cm^{-3}. As illustrated by Fig. 4, thin graded-band MCT layers were provided on both sides of the grown MCT film to suppress the surface recombination of charge carriers at its boundaries.

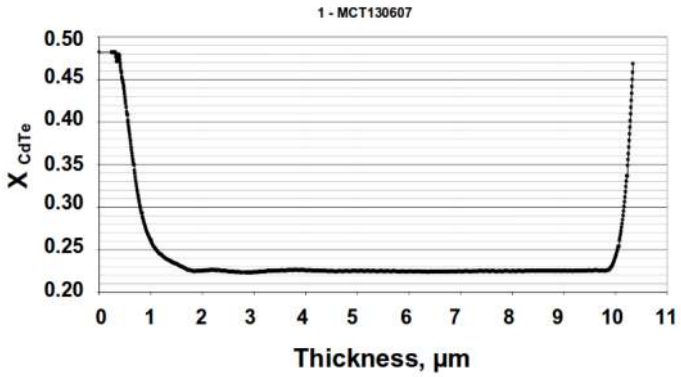

Figure 4. Composition of MCT material over the film thickness.

2.4. Experimental results

Current-voltage characteristics of the diode pairs involving neighbor diodes with different radii of cap contacts were measured, and the photocurrent values were determined from measured data. Results obtained for a diode pair with cap-contact radii R_1 = 10 μm and R_5 =70 μm are illustrated in Fig. 5.

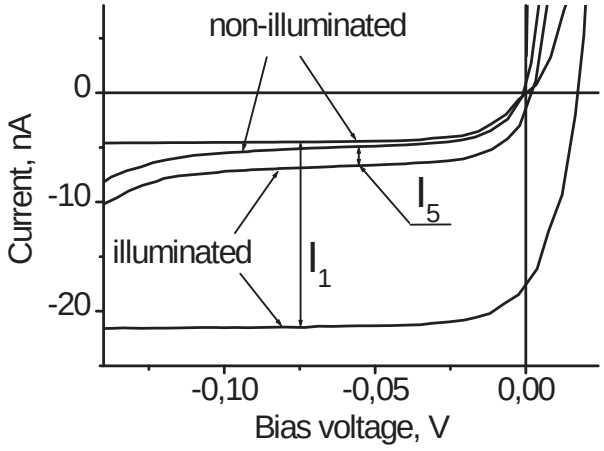

Figure 5. Current-voltage characteristics of a diode pair with cap-contact radii R_1= 10 μm and R_5 =70 μm.

Evidently, the photocurrents I_1 and I_5 remained roughly constant throughout the interval of low bias voltages till the bias voltage -150 mV. In addition, we have $I_1 >> I_5$, which relation proves that the peripheral MIS regions of the photodiodes induced no substantial contribution to measured photocurrent values. Typically, photocurrents were calculated at a bias voltage of

http://dx.doi.org/10.5772/60717

-50 mV. A bar chart of photocurrents I_1 and I_5 for seven diode pairs with cap-contact radii 10 and 70 μm is shown in Fig. 6. Here, the average photocurrent ratio I_1/I_5 equals 9.84.

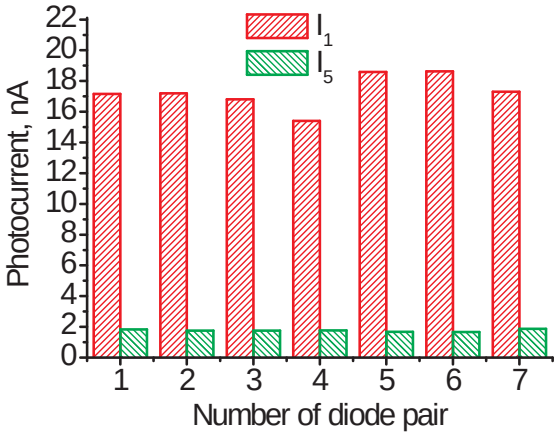

Figure 6. A bar chart of measured photocurrents for diode pairs comprising photodiodes with cap-contact radii 10 and 70 μm.

The theoretically calculated ratios of the photocurrents produced by a diode with the *k*-th shield (*k* = 2÷6) (see Table 1) and by a diode with shield 1 are shown in Fig. 7; as explained above, the photocurrent ratios were calculated by solving Eq. (1). For the dimensions of the *p-n* junctions, the following values were adopted: radius r_0=6.5 μm, inward extension of the *p-n* junction in depth of the MCT film z_0=2 μm. The thickness of the *p*-type absorber film was assumed to be *H*=8 μm. The effective rate of surface recombination of excess carriers on both surfaces of the MCT film was assumed to be zero due to the presence of band-graded MCT layers on those surfaces (see Fig. 4). The absorption of IR radiation in the band-graded MCT layers was neglected.

k	R_k, *μm*	I_1/I_k	L_n , *μm*
1	10	1	
2	17	1.2	22.7±5.3
3	24	1.55	20.4±2.1
4	40	2.88	20.2±0.9
5	70	9.84	20.5±0.8
6	100	23.8	22.8±0.3

Table 1. Measured photocurrent ratios for diode pairs comprising diodes with different cap-contact radii and the determined diffusion-length values L_n.

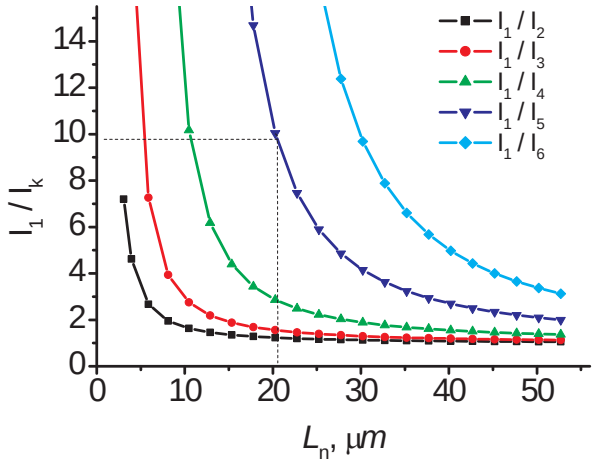

Figure 7. Calculated photocurrent ratios I_1/I_k versus the diffusion length L_n.

Each of the curves in Fig. 7 has an abruptly descending portion appropriate for determining diffusion-length values in a particular interval of L_n.

2.5. Determination of the diffusion length L_n

With reference to the properly chosen curve in Fig. 7, the experimentally measured photocurrent ratio $I_1/I_5 = 9.84$ translates into a diffusion-length value 20.5 μm. Photocurrent ratios I_1/I_k for the diode pairs which comprised diodes with other values of cap-contact radii have also been measured. The values of L_n obtained from the comparison of measured with calculated photocurrent ratios for those diodes are listed in Table 1. The inaccuracy in determining the length L_n can be evaluated considering the scatter of measured ratios I_1/I_k for used photodiodes, whose total number for each shield radius R_k typically amounted to 7. It is seen from Table 1 that very close data with average values of L_n ranging from 20.2 μm to 20.5 μm were obtained for the diode pairs with cap-contact radii 10 and 24, 10 and 40, and 10 and 70 μm. Here, the data obtained from the photocurrent ratios I_1/I_2 and I_1/I_3 are the least accurate results since the curves in Fig. 4 for those diode pairs exhibit a gently sloping behavior in the range of L_n-value around 20 μm.

Application of the largest shield with R_6 =100 μm yields somewhat overestimated values of L_n due to the absorption, in the shielded region, of the radiation having passed through the MCT film and having been partially reflected from the lower surface of the GaAs substrate. Let us evaluate the effect due to the latter reflection. In the case of an 8-μm thick MCT film, one can readily obtain that, for α=2200 cm^{-1}, the radiation flux reaching the MCT film–substrate interface at wavelength $\lambda=0.9\lambda_c$ will amount to 17 % of the incident radiation flux. For reflection-coefficient value 0.27 at the air–GaAs interface, for the reflected radiation we obtain a value amounting to 3.8 % of the total flux initially incident onto the structure. Evaluation yields an additive to the photocurrent I_k approximately equal to 0.05 I_1. The larger value of I_k

http://dx.doi.org/10.5772/60717

will entail a smaller calculated value of I_1/I_k and, hence, a larger value of L_n extracted from the graph of Fig. 7. Clearly, the contribution due to the mentioned additive to the photocurrent produced by the diode with the k-th shield can be neglected providing that $0.05\ I_1 << I_k$, or $I_1/I_k << 20$. From Table 1, we see that the above condition was obviously violated for k=6.

To summarize, our measurements of the electron diffusion length in the fabricated test structure performed on the diodes with cap contacts considerably differing in size have yielded an average length value $<L_n>$=20.2–22.8 μm. A similar analysis performed for the optimum diode pairs with the photocurrent ratios I_1/I_3 and I_1/I_4, whose dependences on L_n as revealed by calculations proved to be much more steeply sloping in the interval of L_n-values around $L_n \approx 20$ μm, has yielded for the length L_n values ranging in the interval from 19.3 to 21.3 μm (with allowance for the scatter of photocurrent-ratio values obtained for 14 measured diode pairs).

3. Determination of the bulk and local diffusion-length values of charge carriers in the photosensing film of ready MCT IR FPA detectors

Below, we present an analysis of the charge-carrier diffusion process in a photosensing film of MCT 2D IR FPA detectors based on spot-scan measurements of such detectors. The analysis was performed with due consideration given to the fact that the extraction of minority carriers by FPA diodes out of the absorber layer, generally speaking, reduces the lifetime of excess carriers in the photosensitive film of the detector in comparison with the "bare" (without FPA diodes) MCT film, making the diffusion length of those carriers in the film regions with photocurrent suction a shorter *effective* diffusion length $l_{d\,eff}$. If the length $l_{d\,eff}$, whose magnitude depends on the level of diode photocurrents, does not exceed the lateral sizes of the FPA diodes, we may speak of a *local* effective diffusion length of photogenerated charge carriers in the film region under the photodiodes. Below, we show how the bulk and local diffusion-length values of charge carriers in different parts of the FPA structure can be evaluated using the spot-scan data measured for FPA detectors at different levels of diode photocurrents.

3.1. Essence of the method

For evaluating the diffusion length of charge carriers in the photosensitive film of FPA detectors, the spot-scan technique was often used [5–9]. In a spot-scan procedure, the charge-carrier diffusion-length value is deduced from spatial diode photoresponses $S(x)$ measured in the vicinity of a local illumination spot shined onto the FPA (see Fig. 8). However, the important fact that the spot-scan procedure itself largely modifies the distribution of minority carriers in the photosensitive film under measurement conditions with relatively high diode photocurrents has not been given due consideration in previous implementations of spot-scan measurements. It should be additionally mentioned here that not only the scanning diode but also its neighbor FPA diodes, which also produce their own photoresponses during scanning, seriously affect the distribution of photogenerated charge carriers in the scanned region. Like the scanning diode does, in performing scans, the neighbor diodes also continuously change

their position with respect to the excitation spot. The latter circumstance hampers the treatment of spot-scan data if one attempts introducing corrections to gained data for photocurrent suction.

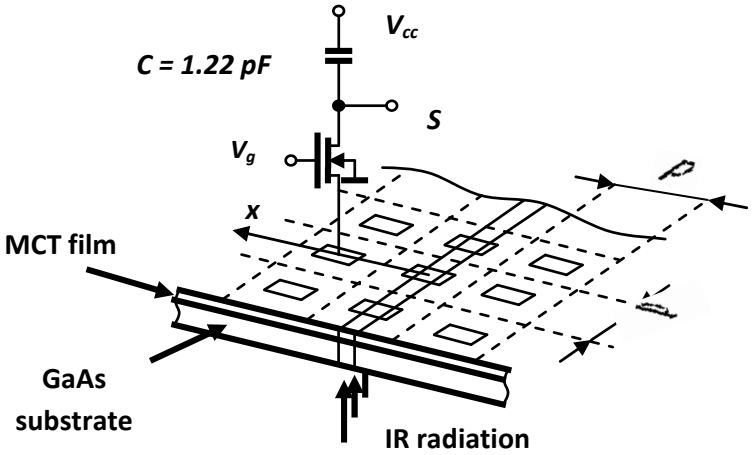

Figure 8. Scanning of a thin-line illumination spot with an FPA photodiode (V_g is the gate potential of the photoelectric-cell input FETs with respect to the frame electrode of the diode array, S is the registered photosignal, C is the storage capacitor, and V_{cc} is the readout integrated circuit (ROIC) supply voltage).

A good strategy toward diminishing the influence of measuring circuits on the distribution of charge carriers in the absorber layer consists in decreasing the level of registered diode photocurrents j_{ph}. By following this strategy, we have recently proposed a new method for determining the bulk diffusion length of charge carriers l_d in the absorber layer of MCT IR FPA detectors [18]. In the new method, the spot-scan technique was implemented at low levels of diode photocurrents j_{ph}, and the bulk diffusion length of charge carriers in the photosensitive film l_d was proposed to be determined as the extreme value of their "spatially averaged" effective diffusion length $\overline{l_{d\ eff}}$ for $j_{ph} \to 0$. The length $\overline{l_{d\ eff}}$ at low diode photocurrents j_{ph} having been sufficiently large, the diffusion of photogenerated charge carriers in the photosensitive film of examined detectors was analyzed in [18] within a continuum approach. At a high level of diode photocurrents j_{ph}, however, the latter approach becomes invalid because of a decreased value of $\overline{l_{d\ eff}}$. In the present paper, we extend the analysis [18] of the diffusion process of charge carriers in the photosensitive film of FPA detectors to the case of large diode photocurrents j_{ph}. We show that, following the determination of the length l_d by the method [18], treatment of spot-scan profiles $S(x)$ measured at large diode photocurrents within a simple 2D diffusion model makes it possible to determine the local effective diffusion length $l_{d\ eff}$ of minority carriers in the film region under FPA diodes in normal operational regime of the photodetector. In this way, we for the first time give a complete analysis of the charge-carrier diffusion process in a photosensitive film of MCT IR FPA detectors at arbitrary diode photocurrents.

http://dx.doi.org/10.5772/60717

3.2. Experimental

In our experiments, two 320x256 $Cd_xHg_{1-x}Te$ *n*-on-*p* photovoltaic detectors with long-wave cutoff wavelengths ~5.4 ($x \approx 0.30$) and ~10 μm ($x \approx 0.225$), hereinafter to be referred to as detectors D-1 and D-2, were used. In both detectors, the diode pitch was $p = 30$ μm, the nominal size of FPA diodes (as defined by the implantation window size in the dielectric) was 10x10 μm, and the thickness of the continuous *p*-type Hg vacancy-doped MCT photosensing layer was about 10 μm. The concentration of acceptors in the absorber layer was $N_a = (7 \div 10) \times 10^{15}$ cm^{-3}. The diode arrays in our detectors were fabricated using boron implantation. Both detectors contained graded-gap wideband MCT layers grown on both sides of the MCT film to ensure surface insulation of FPA diodes and suppress the recombination of charge carriers at the film boundaries [14]. The MCT film of the D-2 detector additionally contained a heavily doped *n*-type MCT layer with a larger bandgap energy provided to it for suppressing the debiasing effect in the diode array [19, 20].

The scanning procedure and the experimental setup used in our experiments are schematically illustrated in Figs. 8 and 9. Different decreased levels of diode photocurrents were implemented by varying the gate-potential value V_g of input field effect transistors (FETs) in the photoelectric cells of the detectors (see Fig. 8). The scans were performed at a 1-μm step by translational displacements of the objective lens installed on a high-precision PC-controlled motorized XYZ-stage. The photoresponse *S* was registered with the help of a shutter controlled by the same personal computer; usually, the photoresponse values were obtained by subtracting the average of typically 10–20 frames taken with closed shutter from the average of the same number of frames taken with open shutter.

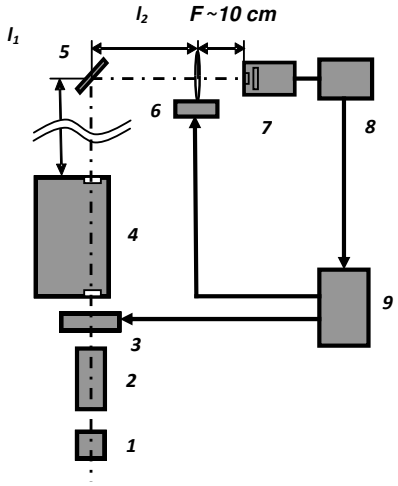

Figure 9. Experimental setup: 1 – globar, 2 – collimator, 3 – PC-controlled shutter, 4 – monochromator, 5 – deflecting mirror, 6 – focusing lens mounted on a motorized XYZ stage, 7 – cryostat with the mounted FPA detector, 8 – electronic equipment controlling ROIC operation and measuring the photoelectric signals, 9 – personal computer.

For diminishing the chromatic aberrations in the objective lens, as the secondary source of IR radiation, we used the exit slit of a monochromator through which IR radiation around wavelengths $\lambda = 4.5$ or 8 μm (respectively, in the case of the D-1 and D-2 detectors) cut off from the globar emission spectrum, passed. Those wavelengths were roughly at the maximum of the spectral sensitivity of the detectors. According to [21], the IR radiation at the above-mentioned wavelengths was absorbed in the absorber layer of the D-1 and D-2 detectors over the characteristic optical lengths $l_{absorp} \approx 0.2$ and 2.4 μm. In the chosen optical configuration, for typical slit-width values of 0.1–0.2 mm, the width of the focused image of the slit at the FPA location in the geometrical optics approximation was smaller than ~8 μm. The diffraction of IR radiation caused some smearing of the slit image on the FPA. The distributions of the illumination intensity $I(x)$ across the excitation spot as implemented in the experiments with the D-1 and D-2 detectors (see Fig. 10, curves 1) were calculated under the assumption that the optical system used in our experiments was a diffraction-limited one, by summing the Airy disc distributions centered at each point of the geometric image of the slit [22]. The manner in which the radiation intensity I diffracted in the vicinity of a strip-like illumination spot of width b was calculated is illustrated by Fig. 11. The calculations of I in the geometrically illuminated region of FPA ($x \le b$) and outside this region ($0 \le x \le b$) were performed by formulas

$$I(x \ge b) = \int_{x+b}^{b} 2r \times Airy(r,\lambda) \times \left[\operatorname{acos}\left(\frac{x}{r}\right) - \operatorname{acos}\left(\frac{x+b}{r}\right) \right] dr + \int_{x}^{x+b} 2r \times Airy(r,\lambda) \times \operatorname{acos}\left(\frac{x}{r}\right) dr,$$

$$I(0 \le x \le b) = \int_{x+b}^{\infty} 2r \times Airy(r,\lambda) \times \left[\frac{\pi}{2} - \operatorname{acos}\left(\frac{b-x}{r}\right) \right] dr + \int_{0}^{b-x} \pi \times r \times Airy(r,\lambda) dr +$$

$$+ \int_{x+b}^{\infty} 2r \times Airy(r,\lambda) \times \left[\frac{\pi}{2} - \operatorname{acos}\left(\frac{b+x}{r}\right) \right] dr + \int_{0}^{b+x} \pi \times r \times Airy(r,\lambda) dr,$$

where $Airy(r, \lambda) = \left(\frac{2J_1(\xi)}{\xi} \right)^2$ is the Airy function ($\xi = 2\pi \frac{D}{\lambda} \theta$, J_1 is the first-kind Bessel function, D is the lens diameter, λ is the radiation wavelength, $\theta = \operatorname{atan}(r/R)$ is the diffraction angle, r is the radius-vector in the plane of FPA, and R is the lens-to-FPA separation).

The experimental conditions that were adopted in measuring the diode photoresponse profiles $S(x)$ in the D-1 and D-2 detectors are summarized in Table 2. For extending, at low and high photocurrent values, the range of photocurrents j_{ph} implemented in our experiments, we used such means as increasing the integration time t_{int} (e.g., from 150 μs to 2 ms in the case of the D-2 photodetector while performing measurements at low currents j_{ph}) or attenuating the illumination intensity in the radiation spot via narrowing the entrance slit of the monochromator (in cases where off-scale swings of the analog-to-digital converter output signal at high photocurrents j_{ph} had to be avoided).

3.3. Results and discussion

Figure 10 shows the wings of the profiles $S(x)$ that were measured at various values of V_g in experiments with the D-1 (curve 2 and symbols 3–5) and D-2 (curve 2 and symbols 3–6)

http://dx.doi.org/10.5772/60717

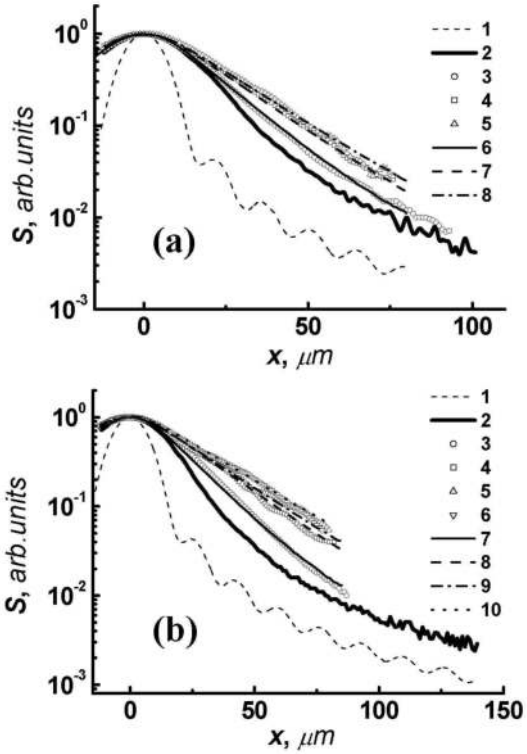

Figure 10. Distribution of the IR radiation intensity in the vicinity of the illumination spot (curve 1) and spot-scan profiles $S(x)$ registered in the D-1 (*a*) and D-2 (*b*) detectors at several values of V_g (the rest data). (*a*) Input-FET gate potential: V_g=1.068 V (curve 2), and 0.96, 0.88, and 0.82 V (symbols 3, 4, and 5 and curves 6, 7, and 8, respectively). Symbols 3–5 and curve 2 show the measured spot-scan profiles $S(x)$; curves 6–8 show the profiles $S(x)$ calculated for small values of V_g by the 1D diffusion model. (*b*) Input-FET gate potential: V_g=0.95 V (curve 2), and 0.90, 0.85, 0.74, and 0.73 V (symbols 3, 4, 5, and 6, and curves 7, 8, 9, and 10, respectively). Symbols 3–6 and curve 2 show the measured spot-scan profiles $S(x)$; curves 7–10 are the profiles $S(x)$ calculated for small values of V_g by the 1D diffusion model.

detectors. As the right and left wings in the measured profiles were slightly asymmetrical, presumably because of some nonuniformity of the recombination properties of the absorber material and because of a slight difference in the electrical characteristics of the neighbor FPA diodes, Fig. 10 shows only the right wings of the profiles, from which data used in subsequent calculations were taken. For clarity, the curves $S(x)$ measured for the D-1 detector in operation with $V_g \leq 0.96$ V and for the D-2 detector in operation with $V_g \leq 0.90$ V are shown in Fig. 10 in a smoothed form. The relation between the as-measured and smoothed profiles $S(x)$ for the noisiest experimental curves (data for D-2 measured at V_g=0.73 and 0.74 V) is illustrated in Fig. 12. It is seen that the case of V_g=0.73 V was the noisiest experimental situation, while already at V_g= 0.74 V the spot-scan profile S(x) was measured quite reliably. The profiles $S(x)$ measured in both detectors at $V_g \leq 0.9$ V are noticeably widened in comparison with the profiles taken from the D-1 and D-2 detectors, respectively, at V_g = 1.086 V and V_g = 0.95 V, that is, at gate-

potential values close to the optimum ones in normal operational regime of the detectors (see Fig. 10). On increasing the gate-potential value in excess of 0.95–1.00 V, the shape of the registered spatial photoresponses exhibited saturation, and the normalized profiles $S(x)$, therefore, remained identical. Wishing to avoid dull data repetition, in Fig. 10 we do not illustrate this fact. Below, we give an analysis to measured profiles $S(x)$ separately for the range of V_g-values in which distinct widening of the bell-shaped profiles $S(x)$ with decreasing the level of diode photocurrents j_{ph} was observed (V_g<0.95–1.00 V) and for the range of V_g-values in which the shape of the profiles $S(x)$ became independent of V_g (V_g>0.95–1.00 V) (conventionally, the cases of small and large diode photocurrents).

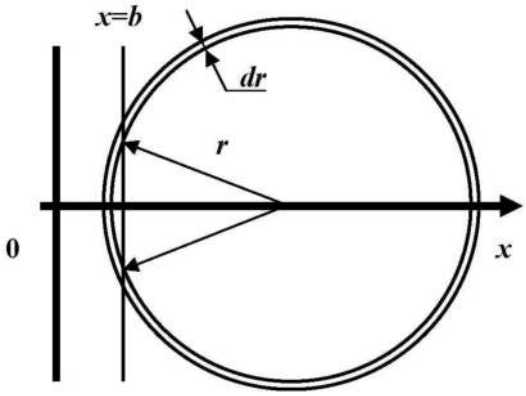

Figure 11. On the calculation of the distribution of the radiation intensity diffracted in the vicinity of an illumination spot shaped as a strip of width b ($0 \le x \le b$), in the region outside the spot ($x \ge b$). The radiation intensity in the region $0 \le y \le b$ was calculated similarly, by summing the contributions due to circular rings and arcs.

D-1 (λ = 4.5 μm)											
V_g, V	t_{int}, μs	I_0, nA	I, arb. units	s, mm	l, cm	D, Cm	F, cm	Δ, Mm	$\overline{l_{d\,eff}}$, μm	$\bar{k}$	$k_{ph\,opt}$
0.82	1300	0.14	1	0.1	214	3.33	10	4.9	17.5	0.24	≈1
0.88	1300	0.2	1	0.1	214	3.33	10	4.9	16	0.485	≈2
0.96	1300	0.5	1	0.1	214	3.33	10	4.9	13	1.25	≈7
1.068	1300	0.29	~0.4	0.1	214	3.33	10	4.9	-	-	≈20-40
D-2 (λ = 8 μm)											
V_g, V	t_{int}, μs	I_0, nA	I, arb. units	s, mm	l, cm	D, Cm	F, cm	Δ, Mm	$\overline{l_{d\,eff}}$, μm	$\bar{k}$	$k_{ph\,opt}$
0.73	2000	0.00026	1	0.2	274	5	10	7.6	24	<0.1	<0.8
0.74	2000	0.0026	1	0.2	274	5	10	7.6	22.5	0.14	≈0.9

http://dx.doi.org/10.5772/60717

0.85	250	0.49	1	0.2	274	5	10	7.6	20	0.44	≈2.5
0.90	150	1.46	1	0.2	274	5	10	7.6	14.5	1.74	≈9
0.95	150	1.68	~0.5	0.2	274	5	10	7.6	-	-	≈20-40

Notation: V_g is the gate potential of photoelectric-cell input FETs with respect to the frame electrode of the diode array, t_{int} is the integration time, I_0 is the photocurrent produced by a photodiode centered at the axis of the illumination spot, I is the IR radiation intensity in the illuminated spot (in arbitrary units different for D-1 and D-2), s is the width of the monochromator exit slit, $l=l_1+l_2$ is the distance from the monochromator exit slit to the lens (see Fig. 9), D and F are the lens diameter and focal length, Δ is the width of the geometric image of the monochromator exit slit at the FPA location, $\overline{l_{d\ eff}}$ is the "spatially averaged" effective diffusion length of minority carriers in the PF of the FPA detector in the model with uniform photocurrent suction, $\bar{k}$ is the value of the coefficient k found in the 1D diffusion model with uniform photocurrent suction, and $k_{ph\ opt}$ is the suction coefficient in the region under the photodiodes in the 2D diffusion model with structured photocurrent suction.

Table 2. Conditions of the spot-scan tests of the D-1 and D-2 detectors and the obtained values of $\overline{l_{d\ eff}}$, $\bar{k}$, and $k_{ph\ opt}$.

3.3.1. The case of small diode photocurrents j_{ph}

As the IR radiation intensity reaching the *n*-regions of the FPA diodes was negligible, the measured diode photoresponses were primarily due to photoelectrons excited by IR radiation in the *p*-type absorber layer and sinking to the *n*-regions of the photodiodes. The spot-scan data obtained at small values of V_g were analyzed within a continuum diffusion model that was developed to clarify the expected asymptotic behavior of $\overline{l_{d\ eff}}$ (j_{ph}) for $j_{ph} \rightarrow 0$. This model could be used because, at the low levels of j_{ph}, we had $\overline{l_{d\ eff}} \geq l_{SCR}/2$ and $\overline{l_{d\ eff}} \geq d$ (here l_{SCR} is the separation between the depletion edges of adjacent FPA diodes and d is the PF thickness) [18].

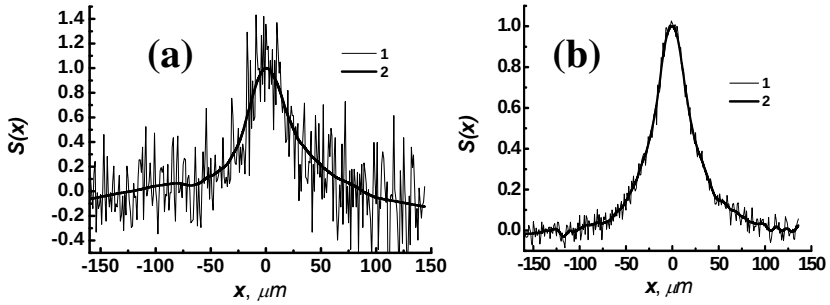

Figure 12. Relation between the most noisy spot-scan curves measured for the D-2 detector at V_g=0.73 (*a*) and 0.74 V (*b*) (curves 1) and their averaged counterparts $S(x)$ (curves 2).

3.3.1.1. Continuum diffusion model. Derivation of the asymptotic $l_{d\ eff} \rightarrow l_d$ for $j_{ph} \rightarrow 0$

The model is based on the following assumptions: (i) the lateral diffusion of the photogenerated charge carriers proceeds in an infinitely thin film; (ii) the photoelectrons are extracted out of the photosensitive film, instead of a discrete diode array, by a large-area electrode continuously

covering the entire surface of the film; (iii) the local photocurrent density j_{ph} varies over the diode area in proportion to the local sheet density of excess minority carriers n_s with a coefficient whose magnitude depends on V_g; (iv) the total photocurrent across the diode can be calculated by integrating the local photocurrent density j_{ph} over the diode area, which has an efficient size t. For our detectors, a value t=14 μm was adopted in the calculations described below (the nominal window size plus 2 μm on either side of the photodiode) [23, 24]. In the formulated model, the spot-scan profiles $S(x)$ can be found by solving the 1D diffusion equation

$$l_d{}^2 \times \frac{\partial^2 n_s}{\partial x^2} - (k+1) \times n_s + g \times \tau = 0,$$

which can also be written as

$$l_{deff}{}^2 \times \frac{\partial^2 n_s}{\partial x^2} - n_s + g \times \tau_{eff} = 0. \tag{2}$$

Here, $l_{d\,eff} = l_d / \sqrt{1+k}$ and $\tau_{eff} = \tau/(1+k)$ are the effective diffusion length and the effective lifetime of excess carriers in the photosensitive film (τ is the lifetime of excess carriers in the bulk absorber material, k is the coefficient that relates the local photocurrent density j_{ph} to n_s, $j_{ph} = k \times n/\tau$), and g is the rate of sheet photogeneration of charge carriers in the photosensitive film. For the normalized profiles $S(x)$, we then have [18]:

$$S(x) = \frac{\int_{x-t/2}^{x+t/2} \left(\int_{-\infty}^{\infty} g(x') \times \exp\left(-\frac{|x'-\xi|}{l_{d\,eff}} \right) d\xi \right) dx'}{\int_{-t/2}^{t/2} \left(\int_{-\infty}^{\infty} g(x') \times \exp\left(-\frac{|x'-\xi|}{l_{d\,eff}} \right) d\xi \right) dx'}. \tag{3}$$

The curves $S(x)$ calculated by formula (3) with the values of $l_{d\,eff}$ providing the best fit of experimental with calculated data for the central part of the bell-shaped spatial photoresponses for V_g=0.73, 0.74, 0.85, and 0.90 V (D-1) and V_g=0.82, 0.86, and 0.96 V (D-2) are shown in Figs. 10(a) (curves 6–8) and 10(b) (curves 7–10). The obtained values of $l_{d\,eff}$, $\overline{l_{d\,eff}}$, are listed in Table 2; in Fig. 13, they are plotted (for fixed illumination intensity in the excitation spot) against the photocurrent I_0 that was produced by the scanning diode when the diode was centered at the spot axis (the current I_0 was evaluated from the maximum photosignal ΔV_0 in the registered scans by the formula $I_0 = C \times \Delta V_0 / t_{\text{int}}$, where C=1.22 pF is the photoelectric-cell charge storage capacity and t_{int} is the integration time).

The curves in Fig. 13 show the dependences $l_{d\,eff}(I_0)$ as predicted by the model; those dependences are defined by a nondimensional parameter $\alpha = (j_0 \times l_d)/G$ that varies in proportion to I_0

http://dx.doi.org/10.5772/60717

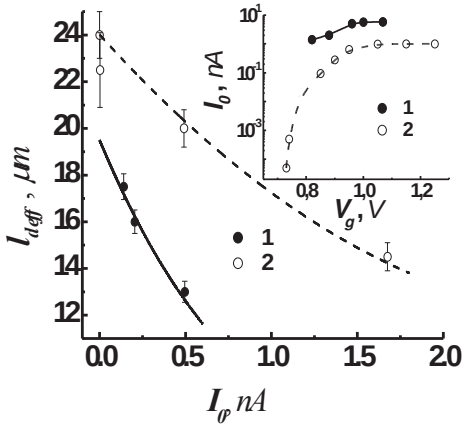

Figure 13. "Spatially averaged" effective minority-carrier diffusion length $\overline{l_{deff}}$ versus the photocurrent I_0 registered by the measuring diode at the maximum of the spot-scan profiles $S(x)$. Symbols 1 and 2 are the data for the D-1 and D-2 detectors; the curves are the dependences calculated by formula (4) with α/I_0=0.9 and 0.33 nA^{-1} for D-1 and D-2, respectively. The inset shows the dependence of I_0 on V_g for the D-1 and D-2 detectors at fixed (yet different for D-1 and D-2) levels of the IR radiation intensity in the illumination spot. Symbols 1 and 2 are the data for the D-1 and D-2 detectors, respectively.

(here $j_0=I_0/(q\times p^2)$ is the average flux of photoelectrons through the spot-centered pixel area (q is the electron charge) and G is the rate of the sheet photogeneration of charge carriers in the illumination spot per unit length of the spot):

$$l_{d\,eff}=l_d\times\left(\sqrt{\alpha^2+1}-\alpha\right)=l_d\cdot\left(1-\alpha+\frac{\alpha^2}{2}+\ldots\right). \tag{4}$$

Formula (4) can be derived as follows. Assuming that $n(x)\propto\exp(\pm x/l_{d\,eff})$, putting $g\approx 0$ outside the spot, and writing the coefficient k as $j_0/(n_0\times\tau)$ (here, n_0 is the sheet density of photogenerated charge carriers in the spot), from Eq. (2) we obtain:

$$\frac{l_d^{\,2}}{l_{d\,eff}^{\,2}}=1+\frac{j_0\times\tau}{n_0}. \tag{5}$$

Considering now the problem over the scale ~ $l_{d\,eff}$ and treating the distribution of illumination intensity in the spot as a delta-function, from the condition of matching the lateral photocurrents that spread from the spot to the left and to the right, for the photoelectron density n_0 we obtain:

$$n_0=\frac{G\times l_{d\,eff}}{2D}. \tag{6}$$

On substitution of expression (6) into relation (5), for $x = \frac{l_{d\,eff}}{l_d}$ we then derive a quadratic equation whose solution yields formula (4).

According to the asymptotic of (4), at low currents I_0 the effective diffusion length $l_{d\,eff}$ decreases quasi-linearly with increasing current I_0 in such a way that the slope α/I_0 defines simultaneously the weakly nonlinear behavior of $l_{d\,eff}(I_0)$. As it is seen from Fig. 13, both conclusions fairly well agree with the experimental data. Interestingly, from the found value of α/I_0 one can readily obtain an estimate of G.

The 1D continuum model described above possesses the following advantageous features: (i) in treating the withdrawal of charge carriers out of the photosensitive film, this model permits leaving aside such things as boundary conditions for the minority carrier concentration n, which would be dealt with in the 3D diffusion model; (ii) the model explicitly involves a quantity $l_{d\,eff}$ whose asymptotic value at low photocurrents gives the bulk diffusion length of minority charge carriers l_d in the photosensitive film; (ii) the model admits derivation of an analytical expression for the asymptotic behavior of $l_{d\,eff}(j_{ph})$ as $j_{ph} \rightarrow 0$.

3.3.1.2. Evaluation of the length l_d in the absorber layer of the examined IR FPA detectors

Approximation of the curve $l_{d\,eff}(I_0)$ to I_0=0 according to asymptotic (4) yields for l_d a value of 19.5 μm in the absorber material of the D-1 detector and a value of 24 μm in the absorber material of the D-2 detector. Those values are in good agreement with relevant data that were previously reported in the literature (see, e.g. [5, 13, 25], where the values of 19 μm [25], 20–23 μm [13], and 25–35 μm [5] were reported for the carrier diffusion length l_d in *p*-type MCT at 78 K), and also with the diffusion-length values calculated from the lifetime and mobility data for *p*-type MCT of similar stoichiometry (see, e.g. [26], where the lifetime and mobility values τ=10–15 ns and μ_e=6.8×10^4 cm^2/V×s, translating into l_d=21.4–26.2 μm, were obtained for a $Cd_xHg_{1-x}Te$ material with x=0.20–0.23).

It would also be instructive to correlate the diffusion-length data obtained in the present study with the available minority-carrier lifetime data for Hg-vacancy-doped MCT. According to [27], the lifetime of excess carriers in the *p*-type $Cd_xHg_{1-x}Te$ material with x=0.225 and 0.30 doped with Hg vacancies to a concentration of (7–10)x10^{15} cm^{-3} is approximately τ=2-4 and 5.5–10 ns. Evaluating the electron mobility in MCT by traditional formulas [21], we obtain the mobility values μ_e=1.06x10^5 and 4.46×10^4 cm^2/V×s for such materials. Then, for the electron diffusion length, we obtain the values of 12–17 μm and 13–18 μm, which fairly well compare with the values of 19.5–24 μm obtained in our detectors. Thus, the diffusion-length values for MWIR and LWIR detectors differ little, in line with the results reported in [16]. Thus, here again we have a good agreement with the literature.

It should be additionally noted here that, as a result of the neglect of the film thickness in the applied approach, our analysis of the profiles $S(x)$ yields somewhat underestimated values of l_d because, for reaching a photodiode, the photogenerated charge carriers, apart from moving laterally, have to diffuse a distance of d across the photosensitive film. However, this underestimate of l_d is of the order of $\vartheta\,(d^2/l_d^2)$; in the case under consideration, it does not exceed ~

http://dx.doi.org/10.5772/60717

2–2.5 μm and can be considered small. Another point that should be mentioned here with reference to Fig. 10 is that for low gate voltages $S(x)$-data become less complicated and more prone to be fit, in an extended range of x, with a single exponential behavior. Fitting the $S(x)$ data for our photodetectors with a single exponential decay constant yields values of $l_{d\,eff}$ that well coincide (within ~1–1.5 μm) with the values of $l_{d\,eff}$ obtained from the calculations based on formula (3).

3.3.2. The case of large diode photocurrents j_{ph} (normal operational regime of FPA detectors)

At currents $I_0 \geq 0.5$ nA/pixel in the D-1 detector and ≥1.5 nA/pixel in the D-2 detector, the length $\overline{l_{d\,eff}}$ becomes comparable with the characteristic lateral size of the diode-array structure l_{SCR}, making it necessary to take the nonuniformity of that structure into account in calculating the diode photoresponses S. Moreover, at large diode photocurrents, the local effective diffusion length of minority carriers in the region under the back-biased diodes $l_{d\,eff}$ becomes comparable with d, and the second applicability condition of the 1D diffusion model, $l_{d\,eff} > d$, also becomes violated. Disregarding, for the time being, the second circumstance, in our analysis of spot-scan data we tried to allow for the discrete structure of the FPA by performing calculations of 2D distributions of the excess carrier concentration $n(x,y)$ in our locally illuminated photodetectors within a 2D diffusion model with d=0 presenting an extension of the previously used 1D diffusion model to the case of two lateral dimensions.

3.3.2.1. 2D calculations

The 2D distribution of the sheet density of photogenerated charge carriers in the photosensitive film of the IR FPA detectors $n_s(x,y)$ with $g(x) \propto I(x)$ was calculated as the solution of the 2D diffusion equation

$$l_d^{\,2} \times \left(\frac{\partial^2 n_s(x,y)}{\partial x^2} + \frac{\partial^2 n_s(x,y)}{\partial y^2} \right) = -g(x) \times \tau + n_s(x,y) + k_{ph} \times P(x,y) \times n_s(x,y). \quad (7)$$

In Eq. (7), the discrete structure of the diode array was taken into account via the function $P(x, y)$, which was assumed to be unity in the region under the FPA diodes and zero in the region outside the FPA diodes. We thereby assumed that, over the area occupied by the FPA, the local diffusion length of charge carriers in the region outside the diodes was equal to l_d. In the region under the diodes, a smaller value of the local (effective) diffusion length, $l_{d\,eff}$, defined by a value of k_{ph} to be found via the fit of calculated to experimental spot-scan data, was assumed. [Here, we would like to remind the reader that under the local diffusion length at a point of interest, we everywhere understand the average distance the charge carriers would move in the absorber material if they were spreading from that point in a spatially uniform photosensitive film with recombination properties of the absorber material being everywhere identical to the recombination properties of the material at the point under consideration. Under the effective diffusion length $l_{d\,eff}$, we understand the diffusion length of charge carriers defined, in addition to their bulk recombination in PF (which, taken alone, defines the value of l_d), also by the

disturbing action due to FPA diodes. The notion of local effective diffusion length of charge carriers, whose meaning can be comprehended by combining the above two definitions, is a notion pertinent to the 2D diffusion model with d=0 used in the present analysis].

The equation was solved by using the MathCad function *relax* in a 1024x1024-μm square domain covered by a square grid whose mesh size was 1 μm. The illumination spot with the distribution of illumination intensity $I(x)$ stretched in the middle of the calculation domain along the y axis. At the calculation-domain boundaries parallel to the centerline of the spot, zero boundary conditions were adopted for the sheet density of excess carriers (n_s=0). The starting boundary conditions at the domain boundaries normal to the illumination spot were initially taken from the solution of the related 1D diffusion problem, and then, at a second iteration made to refine the solution, from the condition of periodicity of the solution in the spot-parallel direction. Afterward, proper integration (over a 14x14-μm square) was used to calculate the relative values of S for various positions of the illumination spot with respect to the scanning diode. As an example, Fig. 14 shows the 2D plots and contour lines of the solutions $n_s(x,y)$ obtained in calculations with k_{ph}=40 for the case in which the scanning diode in the D-2 detector was at the centerline of the illumination spot (Fig. 14 (a)) and for the case in which its center was displaced from the spot axis by 10 μm (Fig. 14(b)). The purpose of our 2D calculations was to find such values of k_{ph} at which the best coincidence between the normalized calculated and experimental diode photoresponse profiles $S(x)$ could be achieved for the experimentally implemented values of V_g, including those for the normal operational regime of the detectors.

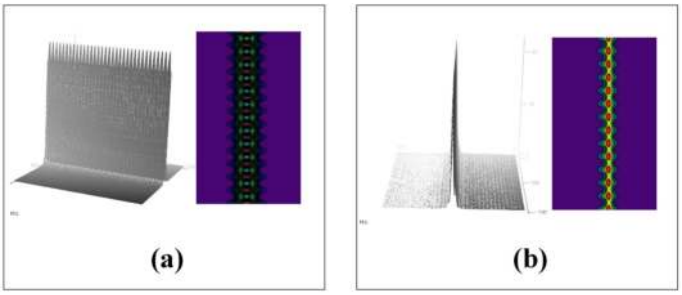

Figure 14. 2D plots and contour lines of the sheet density of excess minority carriers n_s for the measuring-diode position at the centerline of the illumination spot (*a*) and for the diode-center position 10 μm aside from the spot axis (*b*). The data were obtained for the D-1 detector in the calculation with k_{ph}=40.

3.3.2.2. Calculated data and their comparison with the measured spot-scan profile S(x)

The found values of k_{ph}, $k_{ph\ opt}$, are listed in the last column of Table 2. The values of $k_{ph\ opt}$ found for the D-1 detector in operation with V_g≤0.90 V and for the D-2 detector in operation with V_g≤0.95 V proved to be 4–5.5 times greater than the optimal values of the coefficient k, $\bar{k}$, found in the continuum model of [18] with uniform current suction. With the factor 4–5.5 being close to the ratio between the pixel and diode areas, it can be concluded that both models, the model

http://dx.doi.org/10.5772/60717

with continuous photocurrent suction and the model with structured photocurrent suction, yield adequate descriptions to the data measured at small values of V_g providing that one and the same average photocurrent density on the area occupied by the FPA is assumed. The latter result can be regarded as verification of the applicability of the approach of [18] to the analysis of spot-scan data obtained for reduced potentials V_g. For values of V_g typical of the normal operational regime of the detectors (V_g=1.086 V for D-1 and V_g=0.95 V for D-2), the shape of the spatial diode photoresponses $S(x)$ proves to be more complicated in comparison with the profiles $S(x)$ measured at reduced values of V_g, with the wings of the profiles $S(x)$ being less prone to fitting with a single-exponential behavior (Fig. 10). A comparison between the spot-scan profile measured at V_g=0.95 V for the D-2 detector and the profiles $S(x)$ calculated for the same detector by the 2D model with k_{ph} =20, 40, and 60 is given in Fig. 15. Evidently, with k_{ph} ≈ 20-40, a good agreement between the measured profile and the calculated spot-scan profiles was achieved, which shows that, at least in some practically important cases, the model with d=0 is also capable of providing a satisfactory approximation of the measured with calculated profiles $S(x)$ for the values of V_g typical of the normal operational regime of the detectors.

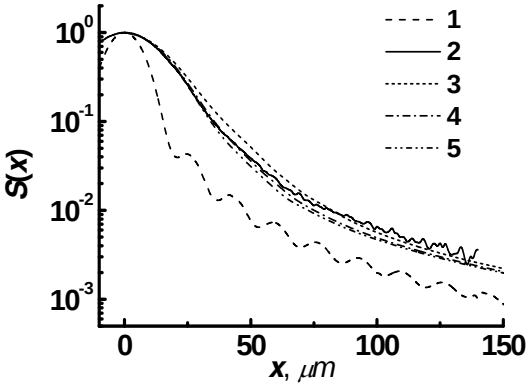

Figure 15. Spot-scan profile $S(x)$ in the D-2 detector measured at V_g=0.95 V (curve 2) in comparison with the profiles $S(x)$ calculated by the 2D diffusion model with k_{ph}=20, 40, and 60 (curves 3, 4, and 5, respectively). Curve 1 is the distribution of the IR radiation intensity.

The above values of k_{ph}, $k_{ph\ opt}$ ≈ 20–40, refer to the effective diffusion-length values of charge carriers in the region under the photodiodes $l_{d\ eff} = l_d / \sqrt{1 + k_{ph\ opt}} \approx 3.7–5.2$ μm. It should be noted here that the above-described fitting procedure yields an upper-type estimate for $l_{d\ eff}$ because, with increasing the magnitude of k_{ph} over $k_{ph\ opt}$ ≈ 20–40, the calculated photoresponses S (and also the shape of the profiles $S(x)$) proved to be weakly dependent on k_{ph}, exhibiting saturation in the vicinity of the measured S-values. Yet, it can be shown that the obtained values $l_{d\ eff}$ ≈ 3.7–5.2 μm agree well with a theoretical estimate of the length $l_{d\ eff}$ (see below). Such an *a priori* estimate of the length $l_{d\ eff}$ in the region under photodiodes can be obtained due to the fact that the values of the second derivatives of the excess carrier concentration n in the lateral direction normal to the spot axis and in the direction across the absorber layer are interrelated

by the 3D diffusion equation, while some plausible assumptions about the shape of the cross-film distributions $n(z)$ can be adopted.

3.3.2.3. A priori estimate of the length $l_{d\,eff}$ under the back-biased photodiodes

The main idea behind the spot-scan method consists in examining the spot-scan profiles $S(x)$ in the film region at the spot edges, where the illumination intensity I rapidly decreases to allow the shape of the formed distributions $n_s(x)$ and $S(x)$ to be largely controlled by the diffusion of charge carriers. A characteristic feature of those areal parts of the photosensitive film is that the excess charge carriers appear in those areal parts predominantly due to their lateral diffusion out of the adjacent film regions (and not due to photogeneration). For those film regions, an *a priori* estimate of $l_{d\,eff}$, which can be used for verification of the found values of $l_{d\,eff}$, can be obtained.

Indeed, let us consider an extended (with a characteristic size $l \gg l_{d\,eff}$) region of an MCT film under a large-area back-biased photodiode. We assume that photogeneration of charge carriers in this region is negligible, and excess carriers enter this region through its lateral boundary parallel to a nearby elongated illumination spot. At a fixed distance from the spot axis (x=const), the function that describes the distribution of the excess carrier concentration across the film (over the z coordinate) can be expanded in a series of sines of the type $\sin[\frac{z}{d_{eff}} \times (\frac{\pi}{2} + 2\pi \cdot n)]$, n=0,1..., which all satisfy the boundary conditions at the film boundaries ($n \approx 0$ at z=0 and $\partial n / \partial z = 0$ at $z \approx d_{eff}$). Here d_{eff} is the effective thickness of the photosensitive film in the region under the FPA diodes (the actual film thickness d minus the sum of the inward extension of the p-n junction in depth of the absorber layer ($d_{deep} \approx 2$–3 μm) and a length of order of the optical absorption length of IR radiation in the absorber material $l_{absorp} \approx 2.4$ μm, see above). Solving the 3D analogue of Eq. (7) by the variable separation method, we see that each component in the series decays exponentially in the PF plane along the x coordinate, the characteristic length of the decay being

$$l_{decay}^{(n)} = l_d \Big/ \sqrt{1 + \left[\frac{l_d}{d_{eff}} \times \left(\frac{\pi}{2} + 2\pi \times n \right) \right]^2} \,. \tag{8}$$

The length l_{decay} for the least rapidly decaying component with n=0, which can be expected to dominate the whole series far enough from the source boundary, should be identified as the effective lateral diffusion length of charge carriers in the photosensitive film $l_{d\,eff\,lat}$. For several realistic values of d_{eff} in the D-2 detector, d_{eff}=6, 7, and 8 μm, formula (8) yields $l_{d\,eff} \approx \frac{2d_{eff}}{\pi} = 3.8$, 4.4, and 5.0 μm, respectively (the approximate equality holds if $(l_d / d_{eff})^2 >> 1$). The above values of $l_{d\,eff\,lat}$ translate into $k_{ph} \approx 22$–39 (here we can use the relation $l_{d\,eff} = l_d / \sqrt{1 + k_{ph}}$ or, alternatively,

http://dx.doi.org/10.5772/60717

take into account the fact that $k_{ph} = l_d^2 \times \frac{\partial n(z)}{\partial z}\Big/ \int_0^{d_{eff}} n(z)dz \approx (\frac{\pi}{2} \times \frac{l_d}{d_{eff}})^2$ for the harmonic with n=0).

In compliance with expectations, the length $l_{d\ eff\ lat} \approx$ 4–5 μm proves to be comparable with the thickness d_{eff}. A similar estimate of the length $l_{d\ eff\ lat}$, $l_{d\ eff\ lat} \approx$ 4–5 μm, was also obtained for the D-1 detector. Thus, for the film region under back-biased diodes, we obtain a good agreement between the lateral diffusion-length values $l_{d\ eff\ lat}$ deduced from the analysis of the shape of the photoresponse profile $S(x)$ (namely, from the values of $k_{ph\ opt}$) and the theoretical estimate of this length.

3.3.2.4. Substantiation of applicability of the 2D diffusion model to the description of spot-scan profiles measured in normal operational regime of the photodetectors

Below, we present heuristic considerations that explain why the diffusion model with d=0 has proved capable of rather adequately reproducing the spot-scan data obtained not only at small, but also at large diode photocurrents j_{ph}. As it was noted above, at low diode photocurrents the distribution $n(z)$ flattens across the film, thus making the treatment of the cross-film dimension unnecessary. On the other hand, at high values of j_{ph} (when the photocurrents show saturation with increasing the potential V_g), the concentration n in the vicinity of the back-biased p-n junctions becomes low, and the distribution $n(z)$ can be no longer considered quasi-uniform.

Substantiation of the 2D model with d=0, as used for the description of spot-scan data in the latter case, can be obtained by integrating both sides of the 3D analogue of Eq. (7) across the photosensitive film. For simplicity, we begin our analysis with consideration of a photosensitive film covered by a continuous large-area back-biased photodiode. For the integrated equation to be consistent with Eq. (7), it is required that the term in the integrated equation which results from integration of the Laplacian component $\partial^2 n / \partial z^2$ and takes the boundary condition on the diode side of the film into account would transform to the term of Eq. (7) with the coefficient k_{ph}. In turn, for such a transformation, it is required that the gradient of n along the film-normal direction on the diode side of the film would vary everywhere (in the film region under the photodiode) in proportion to n_s. Indeed, the local photocurrent is to be calculated in the 3D diffusion model by integrating the film-normal gradient of n over the diode area, whereas the 2D model with d=0 assumes that the local photocurrent density varies in proportion to n_s. If the normal gradient of n on the diode side of the film were varying everywhere in a strict proportion to n_s, then the coefficient $k_{ph} = \frac{j_{ph} \times \tau}{n_s} = \frac{D \times \partial n / \partial z \mid_{z=0} \times \tau}{n_s} = \frac{l_d^2 \times \partial n / \partial z \mid_{z=0}}{\int_o^d n(z)dz}$ would retain its constant value throughout the whole film area covered by the photodiode, and the 2D diffusion model would then be capable of reproducing results of spot-scan measurements as adequately as the 3D diffusion model does. However, in reality, perfect proportionality of $\partial n / \partial z \mid_{z=0}$ to n_s everywhere in the film is lacking because different areal parts of the film feature different distributions $n(z)$ formed in compliance with local conditions of the diffusion problem.

With the aim of evaluating the capability of the 2D model in approximating spot-scan data in the film region under a large-area photodiode, let us consider characteristic distributions $n(z)$ typical of different parts of the scanning interval (see Fig. 16). One characteristic case with $n(z) \propto \sin(\frac{\pi}{2} \times \frac{z}{d_{eff}})$ was discussed above; this case will be referred to below as Case 1 (Fig. 16(b)). Another, in a sense, opposite case is represented by a uniformly illuminated film region in which excess carriers appear due to their photogeneration in a thin layer of the absorber material at the film–substrate interface; this case will be referred to below as Case 2. Clearly, in Case 2, the distribution of n across the film is given by a hyperbolic sine, $n(z) \propto \sinh(z / l_d)$ (Fig. 16(a)). Similarly to Case 1, for which we have found that $k_{ph}^{(1)} \approx (\frac{\pi}{2} \times \frac{l_d}{d_{eff}})^2$, we can calculate the value of k_{ph} for Case 2 as well; then, we obtain: $k_{ph}^{(2)} = (2 \times (\sinh(\frac{d_{eff}}{2l_d}))^{2})^{-1}$, so that we have $k_{ph}^{(2)} \to 2(\frac{l_d}{d})^2$ in thin films with $d/l_d \ll 1$. The latter value of k_{ph} quite moderately (within a factor $\xi = \pi^2/8$) differs from the value of k_{ph} that was obtained for Case 1. It can be suspected that in intermediate cases, in which photogeneration of charge carriers and their diffusion make comparable contributions to the density n_s in the film region of interest, the coefficient k_{ph} will take values from the interval between $k_{ph}^{(2)}$ and $k_{ph}^{(1)}$. The near-unity magnitude of ξ explains why the 2D diffusion model provides a good approximation to the 3D diffusion model in describing the profiles $n_s(x)$ formed in the film region under a continuous back-biased photodiode far enough from the diode edges.

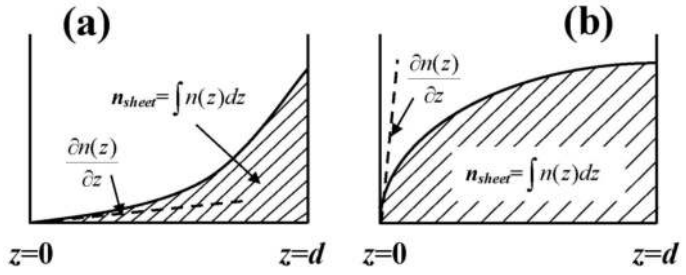

Figure 16. Typical distributions of excess carrier concentration across an MCT film with photocurrent suction in a uniformly illuminated film region (*a*) and in a film region where the excess charge carriers appear due to their lateral diffusion over the film by spreading from a nearby illumination spot (*b*).

In a real FPA structure, the film area occupied by the diode array involves regions with suction of charge carriers (under the back-biased diodes) and no-suction regions (in between the diodes). The excess carriers, as they diffusionally spread sideways from the illumination spot, sequentially pass those alternating regions. As a cloud of charge carriers moves, down the gradient of n_s, past a no-suction region, the distribution $n(z)$ flattens across the film. This flattening results in that there arises an increased fraction of sine harmonics with high spatial

http://dx.doi.org/10.5772/60717

frequencies in the distribution $n(z)$ at the edge of the next diode approached by the cloud of excess carriers; the latter causes an increase in the local photocurrent density at this diode edge in comparison with the value of j_{ph} predicted by the 2D diffusion model as the latter model disregards the evolution of $n(z)$ across the absorber layer. In an improved 2D diffusion model, the increase in the photocurrent density at the diode edge might have been allowed for via a nonuniform distribution of k_{ph} over the diode area, with an increased value of k_{ph} occurring at the diode edge. Apparently, the enhanced rate of withdrawal of charge carriers out of the photosensitive film at the diode edge would result in that, during the further advancement of the cloud in under the photodiode, the extracted local photocurrent will become smaller than the photocurrent predicted by the initial 2D diffusion model with areally uniform value of k_{ph}. It seems that the realistic values of the coefficient k_{ph} and length $l_{d\ eff}$ obtained by fitting the measured spot-scan profile $S(x)$ with the profiles $S(x)$ calculated by the 2D diffusion model result from partial compensation of the two above-mentioned phenomena, this compensation occurring as the scanning photodiode "integrates" the photocurrent density j_{ph} over its own area during spot-scan measurements.

This consideration substantiates the use of the 2D diffusion model for approximating spot-scan data obtained for an arbitrary level of diode photocurrents and explains why this model yields rather realistic local diffusion-length values for the analyzed MCT IR FPA detectors.

3.3.2.5. Refined procedure for determining the length l_d

With the found values $k_{ph\ opt}$, using the solutions $n_s(x,y)$ of the 2D diffusion problem obtained for each value of V_g implemented in our experiments, we can calculate the electron photocurrent $I_{o\ calc}$ that flows across the *p*-*n* junction of the spot-centered measuring diode. In Fig. 17, the calculated values of $I_{o\ calc}$ are compared to the photocurrents $I_{o\ exp}$ that were "measured" by the detector (in Fig. 13, the latter photocurrents, evaluated from the voltage photosignal ΔV_0, were denoted as I_0). The values of $I_{o\ calc}$ were calculated as relative values, and those relative values were subsequently normalized to ensure matching between the saturation levels of the photocurrents $I_{o\ calc}$ and $I_{o\ exp}$ at large potentials V_g (see Fig. 17). An appreciable difference between the two photocurrents observed at reduced potentials V_g for the LWIR FPA D-2 detector (with a smaller bandgap energy of the absorber material) can be attributed to noticeable recombination of photoelectrons with photogenerated holes in the *n*-region of the diode, which approached open-circuit conditions as the potential V_g decreased. Indeed, under such conditions the built-in potential for holes in an illuminated diode loaded to a high-resistance external circuit (high FET-channel resistance) becomes reduced due to accumulation of photoelectrons in the *n*-region (which now cannot be withdrawn into the readout circuit in sufficient amounts), and this reduction provides conditions for a nonnegligible flow of excess holes out of the *p*-type MCT film into the *n*-region, where the holes can recombine with photoelectrons. Under the forward-biased junction, the related electron flux removes photoelectrons out of the cloud of excess carriers diffusionally spreading over the *p*-type photosensitive film; yet, it makes no contribution to the photocurrent "measured" by the detector. The latter circumstance (the existence of an ambipolar flux of excess carriers into the *n*-type diode region out of the *p*-type MCT

film and subsequent recombination of those carriers in this region) violates the previous tacitly adopted assumption that the photocurrent $I_{o\ exp}$ always presents a good approximation to the electron photocurrent being extracted by the photodiodes out of the photosensitive film. Indeed, due to a nonzero rate of "surface recombination" of excess charge carriers on the film surface covered by the photodiode, the electron flux across the *p-n* junction remains finite even as the net photocurrent through the forward-biased photodiode loaded to the high-resistance load tends to zero. This point can be comprehended by considering the diagram of the photocurrent components in the *p-n* junction shown in Fig. 18.

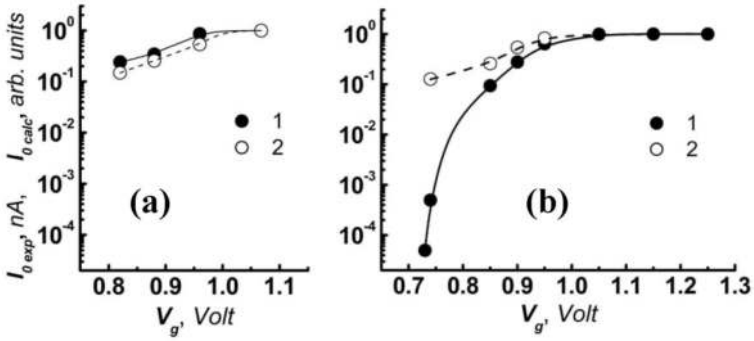

Figure 17. Comparison of the photocurrent values $I_{o\ exp}$ evaluated from the measured voltage photosignals ΔV (*1*) for the spot-centered diode with the photocurrent values $I_{o\ calc}$ calculated by the 2D diffusion model (*2*) for the D-1 (*a*) and D-2 (*b*) detectors. The data for D-2 were normalized to make them refer to the same IR radiation intensity in the illumination spot.

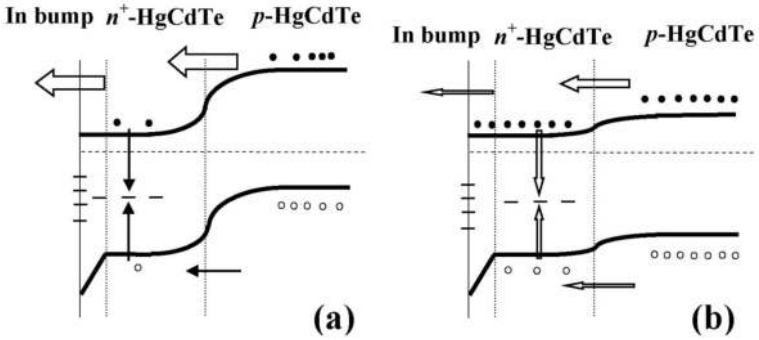

Figure 18. Photocurrent components in the vicinity of a diode junction at a high (*a*) and low (*b*) value of V_g. The diagram illustrates possible occurrence, at low values of V_g, of noticeable recombination of photoelectrons and photoholes in the *n*-type region of the photodiode, the photoelectrons and photoholes having been generated in the *p*-type absorber layer. The arrows show the electron and hole fluxes; the arrow sizes give a rough idea of the magnitude of the shown photocurrent components.

http://dx.doi.org/10.5772/60717

Thus, it is the photocurrent $I_{o\ calc}$ that had to be plotted instead of photocurrent $I_{o\ calc}$ along the abscissa axis in Fig. 13. Within the context of the present study, it is essential that the readily stemming modification of the determination procedure for the length l_d (using $I_{o\ calc}$–values instead of $I_{o\ calc}$–values in plotting the $\overline{l_{deff}}$-vs-I_0 graphs) typically induces quite moderate or even negligible corrections to the initially obtained values of l_d. Indeed, for the D-2 detector the modified procedure yields a value $l_d \approx 25.5$ μm, this length being rather close to the previously obtained value of 24 μm. For the D-1 detector, the modified procedure yields a value of l_d being perfectly coincident with the previously obtained estimate $l_d \approx 19.5$ μm.

4. Conclusions

Two novel methods for determining the bulk diffusion length of minority charge carriers in photosensitive MCT films have been proposed.

The first method, suitable for determining the length l_d in MCT films with suppressed surface recombination of excess carriers, uses tailored diode structures with photodiodes whose vicinity is shielded from incident radiation by a coaxial metal contact. Photocurrent measurements performed on the diodes with different radii of cap contacts can be used to determine the length l_d via a comparison of measured photocurrents with the photocurrents numerically calculated for examined diode configurations. Experimentally, for an Hg-vacancy-doped $Cd_xHg_{1-x}Te$ film with x=0.223 and hole concentration p=6.7x10^{15} cm^{-3} l_d-values ranging between 19 and 23 μm were obtained.

The second method, which can be used for determining the length l_d in the continuous (thickness-uniform, without mesa-isolation of diodes) absorber layers of MCT 2D IR FPA detectors, is based on an analysis of spot-scan data obtained for such detectors at different levels of diode photocurrents. Experimental data gained for n-on-p MCT 2D MWIR and LWIR FPA detectors were analyzed using a 2D diffusion model taking the discrete structure of FPA into account. The properties of the used model were discussed to show that this model could indeed be applied to the analysis of the diffusion process under study. As a result, a general scheme for a comprehensive spot-scan analysis of MCT IR FPA detectors has been proposed. The performed analysis has yielded quite realistic bulk and local diffusion-length values for charge carriers in the film regions under and outside FPA diodes in the examined MWIR and LWIR FPA detectors. Namely, for MCT MWIR and LWIR FPA detectors with long-wave cutoff wavelengths ~5.4 and ~10 μm, for the bulk electron diffusion length the values of l_d≈19.5 и 24 μm were obtained. The latter values comply fairly well with the values obtained by the first method, and they are in a good agreement with relevant data which were previously reported in the literature. Simultaneously, the estimated value of the local diffusion length of minority carriers in the film region under the back-biased FPA diodes, $l_{d\ eff\ lat} \approx$ 4-5 μm, proved to be consistent with a theoretical estimate of this length $l_{d\ eff} \approx \frac{2d_{eff}}{\pi}$, where d_{eff} is the effective PF thickness.

We believe that the newly proposed methods for determining the diffusion lengths of charge carriers in MCT films will add to the toolkit of characterization means for MCT-based IR FPA detectors.

Author details

S.A. Dvoretsky, V.V. Vasil'ev, A.V. Predein, A.V. Vishnyakov, V.A. Stuchinsky*, D.V. Brunev and A.V. Zverev

*Address all correspondence to: stuchin@isp.nsc.ru

Institute of Semiconductor Physics, Russian Academy of Science, Siberian Branch, Novosibirsk, Russia

References

[1] Rogalski A. *Infrared Detectors*. Boca Raton–London–New York: CRC Press, Taylor & Francis Group; 2011.

[2] Aseev A.L., (ed). *Photodetectors Based on the Cadmium-Mercury-Tellurium Epitaxial System*. Novosibirsk: SB RAS Publishing House; 2012.

[3] Levy D., Schacham S.E. Three-dimensional excess carrier distribution in semiconductor imaging array. *J. Appl. Phys.* 1988; 64(10) 5230-5233.

[4] Holloway H. Theory of lateral-collection photodiodes. *J. Appl. Phys.* 1978; 49(7) 4264-4269.

[5] Musca C.A., Dell J. M., Faraone L., Bajaj J., Pepper T., Spariosu K., Blackwell J., Bruce C. Analysis of crosstalk in HgCdTe p-on-n heterojunction photovoltaic infrared sensing arrays. *J. Electron. Mater.* 1999; 28(6) 617-623.

[6] Boltar K.O., Mansvetov N.G., Stafeev V.I., Yakovleva N.I. Inter-element crosstalk in IR focal plane arrays. *J. Opt. Technol.* 2000; 67(2) 153-156.

[7] Sanders T.J., Caraway E.L., Hess G.T., Modeling and test of pixel crosstalk in HgCdTe focal plane arrays. *Proc. of SPIE* 2001; 4369 458-466.

[8] Karp L., Musca C.A., Dell J.M., Faraone L. Characterization of crosstalk in HgCdTe n-on-p photovoltaic infrared arrays. *Proc. of SPIE* 2004; 5274 183-193.

[9] Yinghui S., Bo Z., Nuifang Yu., Oingjin L., Yan Z., Xin W., Peilu J., Xiaoning H., Ning D. Crosstalk of HgCdTe n-on-p diode arrays. *J. Semicond.* 2009; 30(9) 094007-(1-4).

http://dx.doi.org/10.5772/60717

[10] Pultz G.N., Norton P.W., Krueger E.E., Reine M.B. Growth and characterization of *p*-on-*n* HgCdTe liquid-phase epitaxy heterojunction material for 11-18 μm applications. *J. Vac. Sci. Technol.* B 1991; 9(3) 1724-1730.

[11] Reine M.B., Marschoff K.R., Tobin S.P., Norton P.W., Mroczkowski J.A., Krueger E.E. The impact of characterization techniques on HgCdTe infrared detector technology. *Semicond. Sci. Technol.* 1993; 8 788-804.

[12] Predein A.V., Vasil'ev V.V. Method for measuring the diffusion length of minority carriers in semiconductors and a test structure for its realization. Patent RU 2501116 C1, Application No. 2012124443/28, 13.06.2012 (in Russian).

[13] Predein A.V. Application of a test structure with shielded photodiodes for measuring the electron diffusion length in epitaxial *p*-type MCT layers, Proc. of the 23-th ISEC on Photoelectronics and Night Vision Devices, 28-30 May 2014, Moscow, Russia. Moscow: SPA Orion; 2014 (in Russian).

[14] Osadchy V.M., Suslyakov A.O., Vasil'ev V.V., Dvoretsky S.A. Effective lifetime of charge carriers in HgCdTe variband structures. *Fizika i Tekhnika Poluprovodnikov* 1999; 33(3) 293-296 (in Russian).

[15] Vasil'ev V.V., Predein A.V. Influence of graded p-P heterojunction's potential barrier on characteristics of three-dimensional HgCdTe photodiode. *Proc. SPIE* 2005; 5834 83-91.

[16] Varavin V.S., Dvoretsky S.A., Kostyuchenko V.Ya., Ovsyuk V.N., Protasov D.Yu. Mobility of minority charge carriers in p-HgCdTe films. *Semiconductors*. 2004; 38(5) 514-519.

[17] Schacham S.E., Finkman E. Recombination mechanisms in p-type HgCdTe: freezout and background flux effects. *J. Appl. Phys.* 1985; 57(6) 2001-2009.

[18] Vishnyakov A.V., Stuchinsky V.A., Brunev D.V., Zverev A.V., Dvoretsky S.A. Determination of charge-carrier diffusion length in the photosensing layer of HgCdTe n-on-p photovoltaic infrared focal plane array detectors. *Appl. Phys. Lett.* 2014; 104 092112-(1-4).

[19] Varavin V.S., Dvoretsky S.A., Marchishin I.V., Mikhailov N.N., Predein A.V., Remesnik V.G., Sabinina I.V., Sidorov Yu.G., Suslyakov A.O. 320x256 HgCdTe IR FPA with a built-in shortwave cut-off filter. *Opto-Electron. Rev.* 2010; 18(3) 236-240.

[20] Predein A.V., Sidorov Yu.G., Sabinina I.V., Vasil'ev V.V., Sidorov G.Yu., Marchishin V.I. High-performance 320x256 long-wavelength infrared photodetector arrays based on CdHgTe layers grown by molecular beam epitaxy. *Optoelectron. Instrum. Data Process*. 2013; 49(5) 485-491.

[21] Itsuno A.M. Bandgap-engineered HgCdTe infrared detector structures for reduced cooling requirements. Dissertation for the Degree of Philosophy Doctor (Electrical Engineering). University of Michigan; 2012.

[22] Sivukhin D.V. *The General Course of Physics, Vol. 4, Optics*. Moscow: Nauka, 1985 (in Russian).

[23] Vishnyakov A.V., Varavin V.S., Garifullin M.O., Predein A.V., Remesnik V.G., Sabinina I.V., Sidorov Yu.G. Effect of post-implantation annealing on the current-voltage characteristics of IR photodiodes based on p-HgCdTe. *Opto-Electron. Rev.* 2010; 18(3) 236-240.

[24] Vishnyakov A.V., Varavin V.S., Garifullin M.O., Predein A.V., Remesnik V.G., Sabinina I.V., Sidorov Yu.G. Effect of post-implantation annealing on the current-voltage characteristics of IR photodiodes based on p-HgCdTe. *Optoelectron. Instrum. Data Process*. 2009; 45(4), 308-315.

[25] Jung H., Lee H.C., Kim C.K. Measurement of the steady-state minority carrier diffusion length in a HgCdTe photodiode. *Jpn. J. Appl. Phys.* Part 2, 1996; 35(10B) L1321-L1323.

[26] Ikusov D.G., Sizov F.F., Staryi S.I., Teterkin V.V. Recombination mechanisms of non-equilibrium carriers in the $Cd_xHg_{1-x}Te$ (x=0.20 – 0.32) epitaxial layers. *Fizika Tekhnika Poluprovodnikov* 2007; 41(2) 134-139 (in Russian).

[27] Kinch M.A., Aqariden F., Chandra D., Liao P.-K., Schaake H.F., Shin H.D., Minority carrier lifetime in p-HgCdTe. *J. Electron. Mater*. 2005; 34(6) 880-884.